PHYSICAL REVIEW B **87**, 184111 (2013)

Charge disproportionation in $R\mathrm{NiO}_3$ (R = Tm, Yb) perovskites observed *in situ* by neutron diffraction and ^{57}Fe probe Mössbauer spectroscopy

J. A. Alonso[*] and M. J. Martínez-Lope
Instituto de Ciencia de Materiales de Madrid, C.S.I.C., Cantoblanco, E-28049 Madrid, Spain

I. A. Presniakov, A. V. Sobolev, V. S. Rusakov, and A. M. Gapochka
Lomonosov Moscow State University, Leninskie Gory, Moscow 119992, Russia

G. Demazeau
ICMCB-CNRS, University Bordeaux 1 "Sciences and Technologies," Site de l'ENSCBP,
87 Avenue du Dr. A. Schweitzer, 33608 PESSAC Cedex, France

M. T. Fernández-Díaz
Institut Laue-Langevin, B.P. 156, F-38042 Grenoble Cedex 9, France

(Received 20 February 2013; published 17 May 2013)

An *in-situ* investigation from high-resolution neutron powder diffraction data on the structural evolution of TmNiO_3 and YbNiO_3 perovskites across the metal-insulator transition, with $T_{\mathrm{MI}} = 596$ K and 598 K, respectively, allowed the charge disproportionation effect that these perovskites experience upon electronic localization below T_{MI} to be followed. In the insulating (semiconducting) regime, the perovskites are monoclinic, space group $P2_1/n$, containing two inequivalent $\mathrm{Ni1}^{(3+\sigma)+}$ and $\mathrm{Ni2}^{(3-\sigma)+}$ cations; above T_{MI}, the samples become orthorhombic, space group *Pbnm*, with a single site for Ni^{3+}. The ^{57}Fe Mössbauer spectra of iron-doped (at 1.5%) $R\mathrm{NiO}_3$ (R = Tm, Yb) samples recorded below T_{MI} exhibit for Fe1 and Fe2 (replacing Ni1 and Ni2 sites) hyperfine parameters corresponding to large ($\mathrm{Ni1O}_6$) and small ($\mathrm{Ni2O}_6$) octahedra. The remarkable difference between the quadrupole splittings ($\Delta_1 \approx 0.3$ mm/s and $\Delta_2 \approx 0.07$ mm/s) of Fe1 and Fe2 sites in $R\mathrm{Ni}_{0.985}\mathrm{Fe}_{0.015}\mathrm{O}_3$ is analyzed. We calculate the lattice contribution to the electric field gradient (EFG) at ^{57}Fe ions, and estimate, by using the experimental Δ_1 and Δ_2 values, the contributions of the $3d$, $3p$, and $2p$ electrons (overlap distortion and covalence effects). Above T_{MI}, a unique state for iron atoms is observed, upon metallization of the sample.

DOI: 10.1103/PhysRevB.87.184111 PACS number(s): 71.30.+h, 71.45.Lr

I. INTRODUCTION

The systematic study of the metal-to-insulator (MI) transitions in the $R\mathrm{NiO}_3$ (R = rare earths) perovskites, which Torrance *et al.*[1] interpreted as a function of the reduction and closing of the charge-transfer gap between O^{2-} and Ni^{3+} ions, has constituted a recurrent research theme since the 1990s. The difficulty of preparation of these phases, associated with the presence of trivalent nickel, increases as the lanthanide radius diminishes, in such a way that the mentioned transport properties (and MI transitions) had only been investigated for R between La and Eu. Since the work by Demazeau in 1971,[2] the phases for R = Y, Gd, Tb, Dy, Ho, Er, Tm, Yb, and Lu had not been prepared again.

The possibility of synthesizing these materials under moderate pressures of 2 GPa, in closed gold capsules in the presence of KClO_4, in sufficiently large amounts to perform accurate neutron and synchrotron diffraction studies across the transitions, allowed the description for YNiO_3 of a charge disproportionation effect associated with the MI transition.[3,4] This effect is concomitant, in the insulator state, with an extremely subtle monoclinic distortion; in the crystal structure, Ni atoms occupy two independent crystallographic sites with slightly different charge, $3+\sigma$ and $3-\sigma$.

This phenomenon is extensive to other small rare-earth members, from R = Ho to R = Lu.[5,6] The comparative analysis of the structure of the insulator phases at room temperature (RT) demonstrated that, although the monoclinic distortion progressively increases as R size diminishes, the amplitude of the charge modulation seems not to significantly evolve from Ho to Lu.[5] A recent study of the evolution of the charge transfer between $\mathrm{Ni}^{(3+\sigma)+}$ and $\mathrm{Ni}^{(3-\sigma)+}$ for the whole $R\mathrm{NiO}_3$ series from x-ray absorption data[7] suggests that the charge transfer between both Ni states decreases by approaching the itinerant limit and is larger for the heavier lanthanides than suggested in previous studies. This last result generalizes the occurrence of charge disproportionation as an alternative to Jahn-Teller distortions to the dynamic regime, giving further support to recent theoretical work.[8]

The fact that below a critical Ni-O-Ni bond angle there is a stabilization of two distinguishable Ni sites has been alternatively interpreted as a segregation into primarily ionic Ni^{3+}-O bonding at a Jahn-Teller distorted (NiO_6) octahedral site and primarily covalent Ni(III)-O bonding at a less distorted site of smaller mean Ni-O bond length rather than charge transfer between the two Ni sites.[9]

Mössbauer spectroscopy is an invaluable technique with which to provide information concerning the role of the local structure in the global properties of the $R\mathrm{NiO}_3$ family. In preceding papers, the hyperfine parameters of iron-doped nickelates $R\mathrm{NiO}_3$ (R = Nd, Pr, Dy, Lu, Y, and Tl) were reported.[10–14] The ^{57}Fe Mössbauer spectra of nickelates with small (Lu, Y, Tl) and intermediate (Sm, Eu, Dy, Gd) sizes of the R^{3+} cations measured at $T_{\mathrm{N}} < T < T_{\mathrm{MI}}$ were found to consist of a superposition of two subspectra from Fe1 and Fe2, corresponding to the Fe^{3+} cations substituted for nickel in two different Ni1 and Ni2 positions. On the other hand, the ^{57}Fe spectra of nickelates with large rare-earth cations (Pr, Nd) showed the existence of only one Fe^{3+} site, thus suggesting the absence at $T < T_{MI}$ of any disproportionation process in (NiO_6) sublattice. In the case of $LuNi_{0.98}Fe_{0.02}O_3$, for the first time, ^{57}Fe Mössbauer spectroscopy has been applied to following the metal-insulator transition versus temperature.[15] It has been shown that above T_{MI} ($\approx$599 K for R = Lu), the ^{57}Fe spectrum can be described as a single quadrupole doublet. Recently, similar behavior of the ^{57}Fe spectrum was observed by Caytuero *et al.*[16] under detailed Mössbauer studies of iron-doped (1 at.%) nickelate $EuNiO_3$ across the MI transition ($T_{MI} = 460$ K). These results suggest the formation at $T > T_{MI}$ of a unique state for iron probe atoms and could, therefore, imply that the charge disproportionation in nickel sublattice completely disappears.

In this work, we complete this scenario by providing temperature-dependent structural data across the metal-insulator transition in $RNiO_3$ oxides with R = Tm and Yb, previously identified by differential scanning calorimetry (DSC) techniques. We present a detailed study of the structural changes associated with the electronic localization in these distorted perovskites. Also, we report on Mössbauer data in ^{57}Fe-doped samples, clearly showing that $TmNiO_3$ and $YbNiO_3$ also exhibit a charge disproportionation effect below T_{MI}, which vanishes upon metallization of the samples.

II. EXPERIMENTAL

Access at moderate pressures to the metastable $RNiO_3$ oxides requires the careful choice of the starting reactants. Stoichiometric amounts of R_2O_3 (R = Tm, Yb) and $Ni(OH)_2$ were mixed up and ground with $KClO_4$ (30% in weight), introduced into gold capsules (8 mm diameter, 10 mm length), sealed, and placed into a cylindrical graphite heater. The reactions were carried out in a piston-cylinder press (Rockland Research Co.), at a pressure of 2 GPa at 900 °C for 20 min. The decomposition of $KClO_4$ provides an *in-situ* high O_2 pressure that is necessary to stabilize Ni^{3+} ions. The raw products, obtained as dense, homogeneous pellets, were ground and washed in water, in order to dissolve KCl coming from the decomposition of $KClO_4$; then, the powder samples were dried in air at 150 °C for 1 h. The final products were single phase to diffraction measurements.

For the Mössbauer study, the perovskites $TmNi_{0.985}Fe_{0.015}O_3$ and $YbNi_{0.985}Fe_{0.015}O_3$ were prepared in polycrystalline form as follows: analytical grade R_2O_3 (R = Tm, Yb) and $Ni(NO_3)_2{\cdot}6H_2O$ were dissolved in citric acid; a stoichiometric amount of metal ^{57}Fe was previously dissolved in 5 cm^3 of HNO_3 and then added to the citrate solution. The mixtures of citrate and nitrate solutions were slowly evaporated, leading to organic resins, which were dried and decomposed by slowly heating up to 700 °C in air, for 12 h. This treatment gave rise to highly reactive precursor materials, amorphous under x-ray diffraction. The precursor powders were mixed and thoroughly ground with $KClO_4$ (30% in weight), put into gold capsules, sealed, and placed in cylindrical graphite heaters. Then, the high-pressure reactions proceeded as described before.

The products were initially characterized by laboratory x-ray diffraction (XRD) (Cu Kα, $\lambda = 1.5406$ Å). Neutron powder diffraction (NPD) diagrams were collected at the Institut Laue-Langevin (ILL) in Grenoble (France). The crystal structures were refined from high-resolution NPD patterns, acquired below and above the MI temperature at the D2B diffractometer with $\lambda = 1.594$ Å. The samples were placed in a thin-walled vanadium can, inside of a vanadium furnace working at 10^{-5} mPa. NPD data were always collected in a warming-up process. In order to avoid hysteresis-related effects, the temperature was slowly increased (max. 5 °C min^{-1}), and the sample was kept at the target temperature for 30 min before each data collection. In spite of the relatively small amount of sample available (500–800 mg), good-quality patterns were obtained in the high-flux mode. The refinements of the crystal structures were performed by the Rietveld method,[17] using the FULLPROF refinement program.[18] A pseudo-Voigt function was chosen to generate the line shape of the diffraction peaks. The following parameters were refined in the final runs: scale factor, background coefficients,

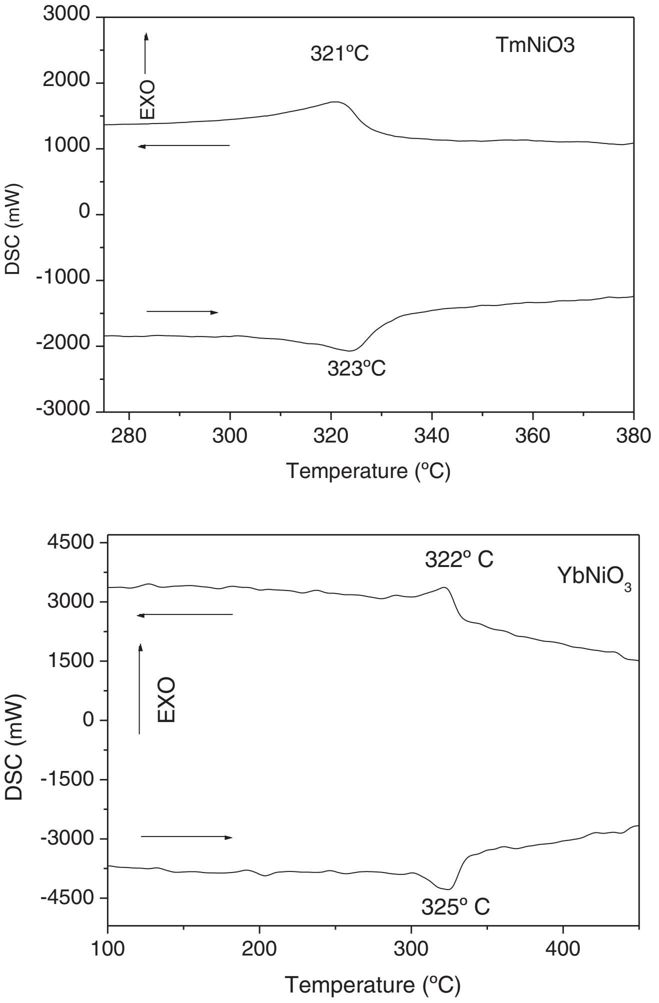

FIG. 1. DSC curves for $TmNiO_3$ and $YbNiO_3$ obtained on the heating and cooling runs.

zero-point error, pseudo-Voigt corrected for asymmetry parameters, positional coordinates, and isotropic thermal factors for all the atoms in the asymmetric unit.

Differential scanning calorimetry (DSC) measurements were performed in a Mettler TA3000 system equipped with a DSC30 unit, in the temperature range from 300 to 863 K. The heating and cooling rates were 10 °C min^{-1}, using about 70 mg of sample in each run.

The ^{57}Fe Mössbauer spectra were recorded at 300–650 K using a conventional constant-acceleration spectrometer. The radiation source ^{57}Co(Rh) was kept at RT. All isomer shifts refer to the α-Fe absorber at 300 K. The experimental spectra were processed and analyzed using methods of spectral simulation and reconstruction of distribution functions of hyperfine parameters corresponding to partial spectra implemented in the *SpectrRelax* program package.[19,20]

III. DSC AND NEUTRON RESULTS

Figure 1 illustrates the DSC curves for TmNiO$_3$ and YbNiO$_3$ obtained during the heating and cooling runs. The heating processes exhibit endothermic peaks centered at 323 °C (596 K) and 325 °C (598 K) for R = Tm, Yb, respectively. The reverse transition, showing exothermic peaks, is observed during the cooling run. By analogy with the DSC peaks observed at the MI transition of precedent members of the RNiO$_3$ family,[3,6,14,21] the peaks shown in Fig. 1 can be assigned to the corresponding MI transitions in RNiO$_3$ (R = Tm, Yb) perovskites. A subtle thermal hysteresis is observed by DSC, suggesting that the transition is weak first order for these strongly distorted perovskites. The heat transfer accounts for the entropy and lattice energy gain due to the electronic delocalization.

TABLE I. Unit-cell, positional, and thermal parameters for RNiO$_3$ (R = Tm, Yb) in the insulating regime, below the metal-insulator transition, refined in the monoclinic $P2_1/n$ space group, $Z = 4$, from NPD data. Reliability factors are also given.

R	Tm			Yb		
T_{MI} (K, heating run)	596			598		
T (K)	295	545	595	295	545	595
a (Å)	5.14535(7)	5.15936(7)	5.16196(7)	5.12979(5)	5.14423(6)	5.14670(6)
b (Å)	5.50378(7)	5.51763(7)	5.52431(7)	5.49957(4)	5.51370(5)	5.52023(5)
c (Å)	7.37508(9)	7.39305(9)	7.38901(10)	7.35370(6)	7.37380(7)	7.37019(8)
β (°)	90.115(1)	90.093(1)	90.068(7)	90.1254(8)	90.1069(3)	90.0870(4)
V (Å^3)	208.854(5)	210.461(5)	210.707(5)	207.459(3)	209.148(4)	209.394(4)
R 4e (x y z)						
x	0.9796(5)	0.9796(5)	0.9798(5)	0.9796(2)	0.9753(2)	0.9795(2)
y	0.0754(2)	0.0757(2)	0.0753(3)	0.0764(1)	0.0765(1)	0.0767(1)
z	0.2503(7)	0.2511(8)	0.2503(11)	0.2496(3)	0.2503(4)	0.2504(5)
B_{iso} (Å^2)	0.27(5)	0.75(3)	0.94(3)	0.30(1)	0.69(2)	0.80(2)
Ni1 2d ($\frac{1}{2}$ 0 0)						
B_{iso} (Å^2)	0.29(5)	0.51(6)	0.80(8)	0.26(4)	0.57(5)	0.60(6)
Ni2 2c ($\frac{1}{2}$ 0 $\frac{1}{2}$)						
B_{iso} (Å^2)	0.20(5)	0.51(6)	0.49(7)	0.26(1)	0.58(5)	0.57(6)
O1 4e (x y z)						
x	0.1046(4)	0.1024(4)	0.1022(4)	0.1074(3)	0.1059(4)	0.1060(4)
y	0.4666(4)	0.4653(4)	0.4659(4)	0.4637(3)	0.4640(4)	0.4646((4)
z	0.2448(5)	0.2456(6)	0.2478(8)	0.2453(4)	0.2455(5)	0.2473(7)
B_{iso} (Å^2)	0.30(4)	0.73(3)	0.87(4)	0.35(3)	0.76(3)	0.92(3)
O2 4e (x y z)						
x	0.6996(7)	0.6973(8)	0.6876(10)	0.6950(5)	0.6957(6)	0.6930(8)
y	0.3106(8)	0.3096(9)	0.3140(9)	0.3123(6)	0.3114(8)	0.3105(10)
z	0.0505(5)	0.0502(6)	0.0478(7)	0.0524(4)	0.0522(5)	0.0525(6)
B_{iso} (Å^2)	0.40(6)	0.85(6)	1.19(9)	0.38(4)	0.77(5)	0.80(6)
O3 4e (x y z)						
x	0.1833(6)	0.1863(7)	0.1959(10)	0.1827(5)	0.1846(7)	0.1886(8)
y	0.2020(7)	0.2023(8)	0.2023(8)	0.2008(6)	0.2007(8)	0.1996(10)
z	0.9455(5)	0.9464(5)	0.9439(6)	0.9446(4)	0.9456(5)	0.9465(6)
B_{iso} (Å^2)	0.27(5)	0.74(6)	0.62(7)	0.44(4)	0.87(5)	0.95(7)
Reliability factors						
χ^2	1.21	1.50	1.50	1.50	2.21	2.41
R_p (%)	3.34	3.08	3.11	3.07	3.40	3.41
R_{wp} (%)	4.18	3.86	3.96	3.86	4.26	4.28
R_{exp} (%)	3.80	3.15	3.24	3.15	2.87	2.76
R_I (%)	4.53	6.44	6.30	3.08	6.10	6.35

The crystal structures below T_{MI} were refined in the monoclinic $P2_1/n$ space group from NPD data, with unit-cell parameters related to a_0 (ideal cubic perovskite, $a_0 \approx 3.8$ Å) as $a \approx \sqrt{2}a_0$, $b \approx \sqrt{2}a_0$, $c \approx 2a_0$. The previously reported RT structures for RNiO$_3$ (R = Ho, Y, Er, and Lu)[5] were used as starting models. For YbNiO$_3$, the presence of minor amounts of NiO and Yb$_2$O$_3$ was considered and introduced in the refinement as second and third phases. In the monoclinic phase, there are two crystallographically independent Ni positions (Ni1 and Ni2), as well as three kinds of nonequivalent oxygen atoms (O1, O2, and O3), all in general positions. (Ni1O$_6$) and (Ni2O$_6$) octahedra alternate along the three directions of the structure, in such a way that each (Ni1O$_6$) octahedron is linked to six (Ni2O$_6$) octahedra, and vice versa. Table I contains the structural parameters from the refinements in the insulating region, from 295 K to a few degrees below the transition temperatures. The β parameter, characterizing the low-temperature monoclinic distortion, is in all cases smaller than 90.13°. Such a small deviation from 90° indicates a strongly pseudo-orthorhombic metric, although the internal monoclinic symmetry, implying the splitting and shifts of oxygen positions around the two Ni sites, is perfectly detected by neutrons, giving rise to a unique and straightforward convergence of the refinements.

Above the transition temperature, the diffraction patterns were refined in the conventional orthorhombic *Pbnm* space group, with a single position for Ni atoms, and two independent positions for oxygen atoms, O1 (*4c*) and O2 (*8d*). Table II contains the atomic coordinates and other refined parameters for the two perovskites in the metallic regime, at temperatures 80–120 K above T_{MI}. As an example, Fig. 2 and Fig. 3 illustrate the good agreement between observed and calculated NPD profiles for TmNiO$_3$ and YbNiO$_3$ perovskites at both sides of the transition. The insets display enlarged regions at high 2θ angle, showing important changes in the diffracted intensities as a consequence of the structural rearrangement across the transition. Tables III and IV list the main interatomic distances and angles for TmNiO$_3$ and YbNiO$_3$ perovskites, respectively.

The main component of the distortion from the ideal cubic perovskite structure corresponds to the tilt of the (NiO$_6$) octahedra, of the type $a^-a^-c^+$ in Glazer's nomenclature, in both $P2_1/n$ and *Pbnm* space groups. Notice that in all cases $c/\sqrt{2}$ lies between b and a, which is the usual situation in perovskites where the primary distorting effect is steric. This distortion is due to the small size of the R^{3+} cations, which forces the (NiO$_6$) octahedra to tilt in order to optimize the R-O distances.

IV. MÖSSBAUER SPECTROSCOPY RESULTS

The ^{57}Fe Mössbauer spectra of the TmNi$_{0.985}{}^{57}$Fe$_{0.015}$O$_3$ and YbNi$_{0.985}{}^{57}$Fe$_{0.015}$O$_3$ samples, measured at T = 295 K ($T \ll T_{\mathrm{MI}}$), are shown in Fig. 4. As in the case of iron-doped nickelates RNi$_{0.99}{}^{57}$Fe$_{0.01}$O$_3$ with intermediate (Sm, Eu, Dy, Gd)[12,14] and small (Lu, Y, Tl)[11,22] size of the R^{3+} ions at $T_{\mathrm{N}} < T < T_{\mathrm{MI}}$, these spectra can be presented as a superposition

TABLE II. Unit-cell, positional, and thermal parameters for RNiO$_3$ (R = Tm, Yb) in the metallic regime, above the metal-insulator transition, refined in the orthorhombic *Pbnm* space group, $Z = 4$, from NPD data. Reliability factors are also given.

R	Tm		Yb		
T (K)	635	685	635	722	817
a (Å)	5.16369(7)	5.16696(7)	5.14861(6)	5.15393(6)	5.16009(7)
b (Å)	5.53219(7)	5.53366(7)	5.53019(5)	5.53270(6)	5.53521(6)
c (Å)	7.38082(10)	7.38628(9)	7.35897(7)	7.36873(8)	7.37992(9)
V (Å^3)	210.844(5)	211.190(5)	209.531(4)	210.120(4)	210.787(4)
R 4c (x y $\frac{1}{4}$)					
x	0.9797(5)	0.9791(4)	0.9797(2)	0.9803(2)	0.9799(2)
y	0.0758(2)	0.0751(2)	0.0770(1)	0.0766(1)	0.0761(2)
B$_{\mathrm{iso}}$ (Å^2)	1.031(3)	0.95(3)	0.91(8)	1.00(2)	1.13(2)
Ni 4b ($\frac{1}{2}$ 0 0)					
B$_{\mathrm{iso}}$ (Å^2)	0.753(2)	0.80(2)	0.70(2)	0.78(2)	0.88(2)
O1 4c (x y $\frac{1}{4}$)					
x	0.1035(4)	0.1028(4)	01052(4)	0.1062(4)	0.1052(5)
y	0.4668(4)	0.4672(4)	0.4650(4)	0.4647(4)	0.4642(4)
B$_{\mathrm{iso}}$ (Å^2)	1.08(3)	1.12(3)	0.94(3)	1.05(3)	1.24(4)
O2 8d (x y z)					
x	0.6925(3)	0.6922(3)	0.6917(6)	0.6912(3)	0.6914(3)
Y	0.3052(3)	0.3057(3)	0.3065(3)	0.3068(3)	0.3066(3)
z	0.0518(2)	0.0517(2)	0.0525(2)	0.0522(2)	0.0525(2)
B$_{\mathrm{iso}}$ (Å^2)	1.09(2)	1.09(2)	1.02(2)	1.12(2)	1.22(3)
Reliability factors					
χ^2	1.40	1.72	2.64	2.51	2.28
R$_{\mathrm{p}}$ (%)	3.00	2.85	3.30	3.33	3.43
R$_{\mathrm{wp}}$ (%)	3.84	3.60	4.17	4.23	4.34
R$_{\mathrm{exp}}$ (%)	3.25	2.75	2.57	2.67	2.88
R$_{\mathrm{I}}$ (%)	6.12	6.09	6.60	6.85	7.88

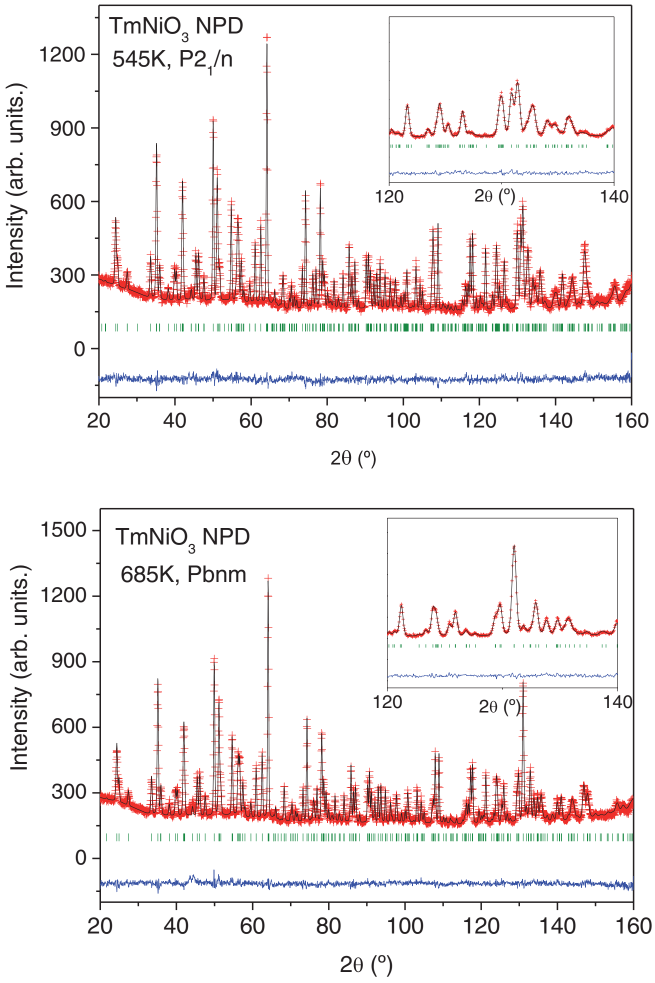

FIG. 2. (Color online) Observed (crosses), calculated (full line), and difference (bottom) NPD Rietveld profiles for TmNiO$_3$ (a) below $T_{\rm MI}$ (monoclinic) and (b) above (orthorhombic) $T_{\rm MI}$. The insets show enlarged high-angle 2θ regions where the effect of the structural rearrangement can be appreciated.

of two quadrupole doublets from Fe1 and Fe2 corresponding to the Fe^{3+} cations substituted for nickel in the Ni1 and Ni2 sites of the monoclinic RNiO$_3$ lattice (at $T < T_{\rm MI}$). The best-fit values of hyperfine parameters for these subspectra (Table V) are in a good agreement with the corresponding data for the other members of RNiO$_3$ ($R = {\rm Sm} - {\rm Lu}$, Y, Tl).[11,12,14,22] It is worth noting that Fe is not a completely harmless dopant, which may lead to a shift of the MI transition by a few degrees. However, within the temperature resolution of the data acquisition, the transitions occur as expected from DSC and NPD measurements.

Figure 4 also includes the most typical spectra of the RNi$_{0.985}$^{57}Fe$_{0.015}$O$_3$ (R = Tm, Yb) nickelates, recorded in the temperature range that contains the temperature of the insulator-metal phase transition for the undoped TmNiO$_3$ ($T_{\rm MI} \approx 596$ K) and YbNiO$_3$ ($T_{\rm MI} \approx 598$ K) samples. A model deconvolution of these spectra was performed at fixed ratio of areas I_1/I_2 for the Fe1 and Fe2 subspectra, determined at $T = 295$ K (Table V), and equal widths (Γ) of all the resonant lines. The temperature dependencies $\delta_{1,2}(T)$ and $\Delta_{1,2}(T)$ are shown in Fig. 5. Upon heating the samples above $T_{\rm MI}$, the Fe1 and Fe2 subspectra are characterized by the same values of the isomer shifts ($\delta_1 = \delta_2$) and quadrupole splittings ($\Delta_1 = \Delta_2$) given in Table V. This result suggests the formation of a unique state for iron atoms within the orthorhombic phase of the TmNiO$_3$ and YbNiO$_3$ samples ($T > T_{\rm MI}$). Lowering the temperature below $T_{\rm MI}$ again results in the two Fe1 and Fe2 subspectra, thus showing the reversibility of observed changes in the Mössbauer spectra.

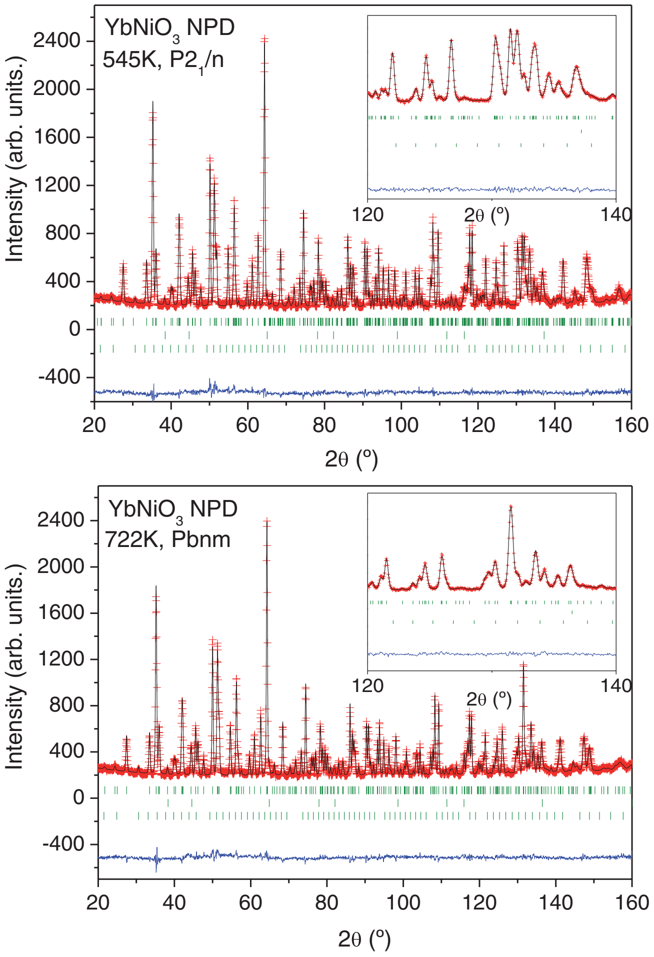

FIG. 3. (Color online) Observed (crosses), calculated (full line), and difference (bottom) NPD Rietveld profiles for YbNiO$_3$ (a) below $T_{\rm MI}$ (monoclinic) and (b) above (orthorhombic) $T_{\rm MI}$. The second and third series of Bragg reflections correspond to NiO and Yb$_2$O$_3$ minor impurities.

V. DISCUSSION

For both TmNiO$_3$ and YbNiO$_3$, the MI transition occurs considerably above RT ($T_{\rm MI} = 596$ and 598 K in the heating run, respectively); these values intercalate in between those of ErNiO$_3$ and LuNiO$_3$, and they give a complete picture of the phase diagram of rare-earth nickelates. Table VI includes the MI transition temperatures for the whole family of RNiO$_3$ perovskites. The phase diagram showing the evolution of $T_{\rm MI}$ as a function of the structural distortion (governed by the R^{3+} size[23]) has been represented in Fig. 6. The MI transition temperature follows the monotonous variation observed for RNiO$_3$ with larger R^{3+} cations, although the

TABLE III. Main bond distances (Å) selected angles (°), and distortion parameters Δ_d for monoclinic and orthorhombic $TmNiO_3$.

T (K)	295	545	595		635	685
Ni1-O1(*x*2)	1.968(4)	1.963(4)	1.946(6)	Ni-O1(*x*2)	1.9298(6)	1.9300(6)
Ni1-O2(*x*2)	2.029(4)	2.023(5)	2.017(5)	Ni-O2(*x*2)	1.996(2)	1.998(2)
Ni1-O3(*x*2)	2.012(3)	2.005(4)	1.970(5)	Ni-O2′(*x*2)	1.957(2)	1.957(2)
⟨Ni1-O⟩	2.003(4)	1.997(4)	1.978(5)	⟨Ni-O⟩	1.961(1)	1.962(2)
Δ_d 10^{-4}	1.65	1.58	2.22	Δ_d 10^{-4}	1.92	2.02
Ni2-O1(*x*2)	1.891(4)	1.901(4)	1.914(6)			
Ni2-O1(*x*2)	1.902(4)	1.919(4)	1.945(5)			
Ni2-O1(*x*2)	1.935(4)	1.944(5)	1.976(5)			
⟨Ni2-O⟩	1.909(4)	1.921(4)	1.945(5)			
Δ_d 10^{-4}	0.96	0.84	0.85			
⟨Ni-O⟩	1.956(4)	1.959(4)	1.961(5)			
Ni1-O1-Ni2	145.782)	146.2(2)	146.3(3)	Ni-O1-Ni	145.95(3)	146.18(3)
Ni1-O2-Ni2	146.8(2)	146.8(2)	145.1(2)	Ni-O2-Ni	146.35(7)	146.26(7)
Ni1-O3-Ni2	145.3(2)	146.0(2)	146.7(2)			

expected variation rate decreases for the last members of the series.

At RT, the structural data for $TmNiO_3$ and $YbNiO_3$ correspond to samples with a 100% of insulating fraction. In the insulating regime below T_{MI} ($P2_1/n$ space group), Ni1 and Ni2 sites alternate along the three crystallographic directions. As shown in Tables III and IV, the mean Ni-O distances in the ($Ni1O_6$) octahedra are considerably larger than in the ($Ni2O_6$) polyhedra at RT; we obtain a picture of expanded and contracted (NiO_6) octahedra alternating along the three axes (left inset of Fig. 6), a consequence of the charge disproportionation phenomenon in the insulating phase. The difference between both mean Ni-O distances is comparable (within the standard deviations) to that previously observed for the other rare-earth nickelates with similar ionic R^{3+} size (R = Y, Ho, Er, Lu).[5]

The analysis of the temperature-dependent diffraction data allowed us to follow the structural changes concomitant with the electronic delocalization as the samples were heated across the MI transition. The diffraction patterns in the RT $< T <$ T_{MI} range are well reproduced using the $P2_1/n$ space group, whereas above T_{MI}, the structure is well described in the *Pbnm* orthorhombic space group. Figures 7 and 8 plot the thermal variation of the unit-cell parameters for $TmNiO_3$ and $YbNiO_3$, respectively. The same pattern of behavior is observed for both oxides, with abrupt changes at the same temperatures where the DSC peaks were observed. The thermal evolution of the unit-cell parameters is very anisotropic. There is an abrupt contraction in the c parameter ($\Delta c \approx -0.012$ Å), whereas b experiences an expansion ($\Delta b \approx +0.015$ Å); the change in the a parameter is comparatively much smaller, showing the same thermal expansion in the whole temperature range. Similar rearrangements of the cell size were observed in former studies for $RNiO_3$ compounds (R = Ho, Y, Er, Lu)[6] and $DyNiO_3$.[14]

Figures 7(b) and 8(b) also illustrate the contraction in the unit-cell volume upon heating across the transition, superimposed onto the expected thermal expansion if no electronic effects were present at T_{MI}. The temperature evolution of the

TABLE IV. Main bond distances (Å), selected angles (°), and distortion parameters Δ_d for monoclinic and orthorhombic $YbNiO_3$.

T (K)	295	545	595		635	722	817
Ni1-O1(*x*2)	1.964(3)	1.966(4)	1.951(5)	Ni-O1(*x*2)	1.9276(6)	1.9317(6)	1.9334(8)
Ni1-O2(*x*2)	2.024(3)	2.028(4)	2.019(5)	Ni-O2(*x*2)	1.999(2)	2.000(2)	2.001(2)
Ni1-O3(*x*2)	2.008(3)	2.002(4)	1.983(5)	Ni-O2′(*x*2)	1.953(2)	1.956(2)	1.957(2)
⟨Ni1-O⟩	1.999(3)	1.999(4)	1.984(5)	⟨Ni-O⟩	1.960(1)	1.962(3)	1.965(2)
Δ_d 10^{-4}	1.61	1.62	1.96	Δ_d 10^{-4}	2.27	2.05	2.04
Ni2-O1(*x*2)	1.896(3)	1.899(4)	1.912(5)				
Ni2-O1(*x*2)	1.914(3)	1.919(4)	1.934(5)				
Ni2-O1(*x*2)	1.937(3)	1.947(4)	1.963(5)				
⟨Ni2-O⟩	1.916(3)	1.922(4)	1.936(5)				
Δ_d 10^{-4}	0.77	1.05	1.16				
⟨Ni-O⟩	1.957(3)	1.960(4)	1.960(5)				
Ni1-O1-Ni2	146.6(1)	145.1(1)	145.1(2)	Ni-O1-Ni	145.28(3)	144.98(3)	145.22(3)
Ni1-O2-Ni2	145.4(1)	145.6(2)	145.3(2)	Ni-O2-Ni	145.86(7)	145.82(7)	145.77(7)
Ni1-O3-Ni2	144.8(1)	145.4(2)	146.0(2)				

TABLE V. Hyperfine parameters obtained from the experimental ^{57}Fe Mössbauer spectra for $R\mathrm{Ni}_{0.985}{}^{57}\mathrm{Fe}_{0.015}\mathrm{O}_3$ (R = Tm, Yb) at $T = 300$ K ($T < T_{\mathrm{MI}}$) and from lattice EFG calculation of quadrupole splittings (Δ_i^{lat}) for ^{57}Fe undoped RNiO$_3$ (R = Tm, Yb) samples.

R	Subspectrum	δ (mm/s)	Δ (mm/s)	Γ (mm/s)	I (%)	$\lvert\Delta^{\mathrm{lat}}\rvert$ (mm/s)
Tm	Fe1	0.27 ± 0.01	0.33 ± 0.02	0.32 ± 0.01	60 ± 3	0.294
	Fe2	0.16 ± 0.02	0.08 ± 0.04		40 ± 3	0.314
Yb	Fe1	0.27 ± 0.01	0.32 ± 0.03	0.34 ± 0.03	59 ± 5	0.295
	Fe2	0.14 ± 0.02	0.07 ± 0.05		41 ± 5	0.272

β angle is also plotted in Figs. 7(b) and 8(b). The deviation from 90° is small (90.115° and 90.125° at RT for Tm and Yb, respectively), but the change to a monoclinic symmetry below T_{MI} is apparent in both compounds. These figures compare with those observed in other RNiO$_3$ (R = Ho, Y, Er and Lu) perovskites, where the observed β angles ranged from 90.08° for R = Y, Ho to 90.16° for LuNiO$_3$ at RT.[5]

It is interesting to follow the evolution of the interatomic Ni-O bonds. The thermal dependence of Ni-O distances obtained from the analysis of the NPD data is displayed in Figures 9 and 10 for R = Tm, Yb, respectively. Figures 9(a) and 10(a) show an abrupt convergence of the two sets (Ni1 and Ni2) of three Ni-O bond lengths in the monoclinic-insulating phase, to three unique Ni-O distances in the orthorhombic-metallic phase. This phenomenology indicates that the charge disproportionation completely vanishes at the MI transition. The two apical Ni1-O1 and Ni2-O1 bond lengths result in a single Ni-O1 distance in the orthorhombic phase. On the *ab* plane, Ni1-O2 and Ni2-O2 bonds converge to Ni-O2, whereas Ni1-O3 and Ni2-O3 converge to Ni-O2′. On the other hand, Figs. 9(b) and 10(b) illustrate the thermal evolution of the mean ⟨Ni-O1⟩, ⟨Ni-O2⟩, and ⟨Ni-O3⟩ bond distances, obtained by averaging the bond distances from Ni1 and Ni2 atoms to every oxygen atom. This allows the thermal dependence of the amplitude of the charge disproportionation effect to be evaluated. This plot suggest a collapse of the charge

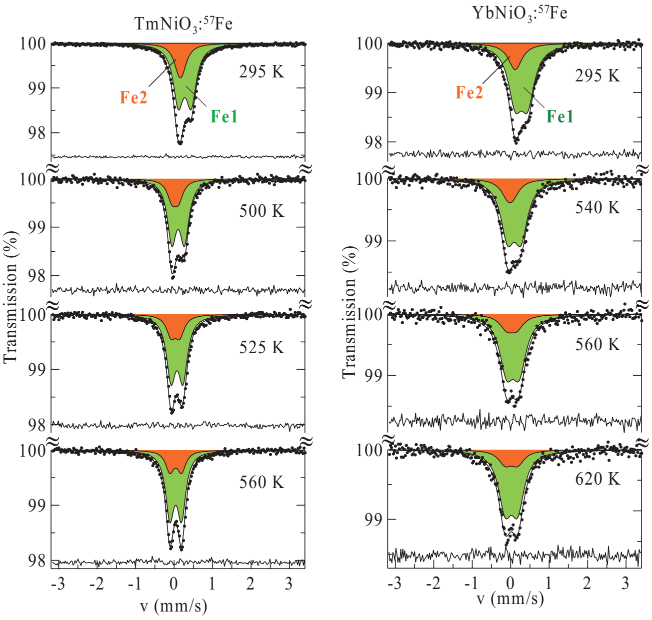

FIG. 4. (Color online) Characteristic ^{57}Fe Mössbauer spectra of the nickelates $\mathrm{TmNi}_{0.985}{}^{57}\mathrm{Fe}_{0.015}\mathrm{O}_3$ and $\mathrm{YbNi}_{0.985}{}^{57}\mathrm{Fe}_{0.015}\mathrm{O}_3$ (300 K $\leqslant T \leqslant$ 700 K).

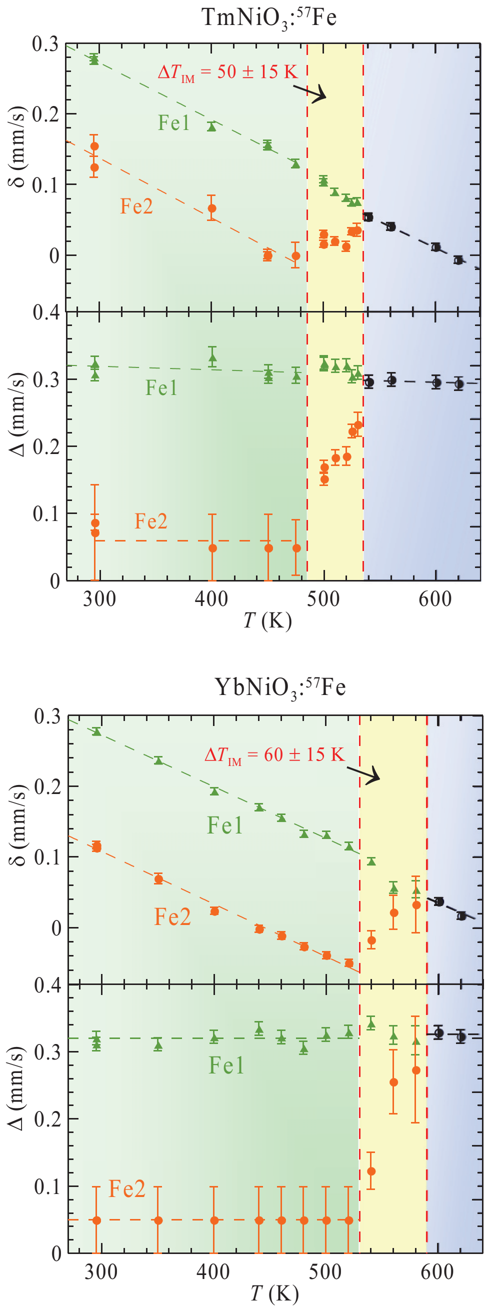

FIG. 5. (Color online) Temperature dependencies of the isomer shifts (δ_i) and quadrupole splittings (Δ_i) for Fe1 and Fe2 subspectra of $R\mathrm{Ni}_{0.985}{}^{57}\mathrm{Fe}_{0.015}\mathrm{O}_3$ (R = Tm, Yb).

TABLE VI. Metal-insulator transition temperatures of the whole family of $RNiO_3$ perovskites, measured from DSC data in the heating run.

R	T_{MI} (K)	References
La	–	1
Pr	130	1
Nd	200	1
Sm	400	1
Eu	463	23
Gd	511	24
Dy	564	14
Ho	573	6
Y	582	3
Er	584	6
Tm	596	This work
Yb	598	This work
Lu	599	6

disproportionation a few degrees below the T_{MI} transition, probably corresponding to a coexistence of the orthorhombic (with a single Ni site) and the monoclinic phase.

It is also worth commenting on the evolution of the distortion of the NiO_6 octahedra across the transition, defined by the distortion parameter $\Delta_d = (1/6)\Sigma_{n=1,6}\,[(d_n - \langle d\rangle)/\langle d\rangle]^2$, also included in Tables III and IV. At RT, the distortion parameters of the large $Ni1O_6$ octahedra (1.65 and 1.61 $\times\ 10^{-4}$ for $R =$ Tm, Yb) are significantly bigger than those of the small ($Ni2O_6$) octahedra (0.96 and 0.77 $\times\ 10^{-4}$ for $R =$ Tm, Yb). This is in connection with the scenario presented by Goodenough *et al.*,[9] where Jahn-Teller distorted (NiO_6) octahedral sites with ionic Ni^{3+}-O bonding alternate with primarily covalent Ni(III)-O bonding at less distorted sites of smaller mean Ni-O bond length. On the other hand, Δ_d increases with temperature and reaches its maximum value at temperatures close to T_{MI}. In particular, values of Δ_d as high as 2.22×10^{-4} ($R =$ Tm) or 1.96×10^{-4} ($R =$ Yb) are observed immediately before the transition. These anisotropic bond distances are maintained upon the electronic delocalization and seem to be characteristic of the small rare-earth nickelates.

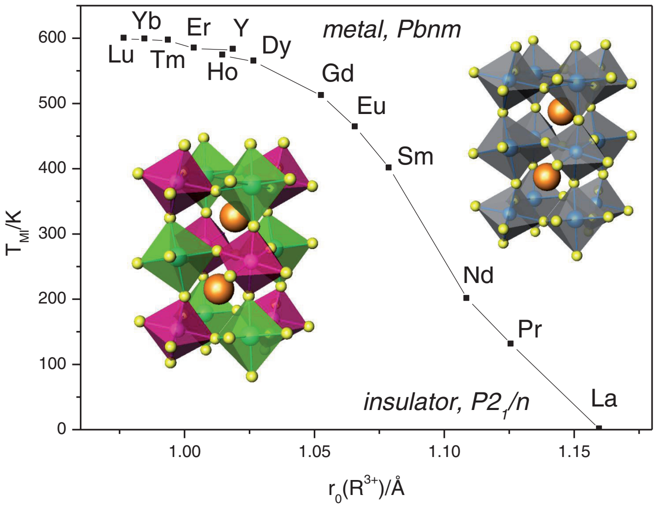

FIG. 6. (Color online) Phase diagram of $RNiO_3$ perovskites showing the boundary between insulator and metallic phases, from DSC data. The inset illustrates the monoclinic (left) and orthorhombic (right) crystal structures; the former contains two distinct sites for Ni.

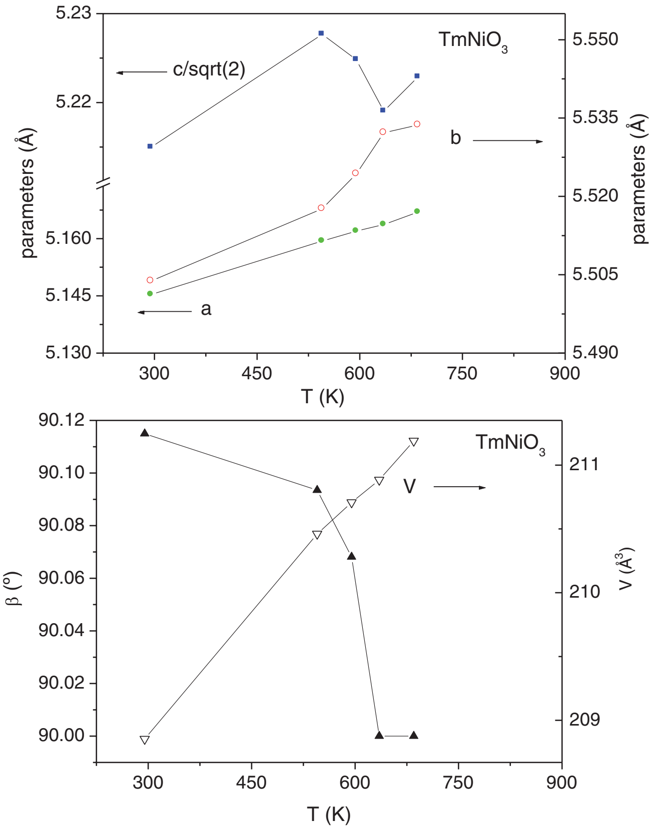

FIG. 7. (Color online) Thermal variation of the unit-cell parameters across the electronic delocalization of $TmNiO_3$ ($T_{MI} = 596$ K). (a) a, b, and c parameters, and (b) monoclinic β angle and unit-cell volume.

The ^{57}Fe Mössbauer spectra of iron-doped $RNi_{0.985}{}^{57}Fe_{0.015}O_3$ ($R =$ Tm, Yb) recorded at $T < T_{MI}$ exhibit two quadrupole doublets (Fig. 4) corresponding to $Fe^{3+}\rightarrow Ni^{3+}$ substitution in ($Ni1O_6$) and ($Ni2O_6$) sites. The difference between δ_1 and δ_2 values ($\Delta\delta \approx 0.12$ mm/s) can be explained by the different character of Fe-O chemical bonds in ($Fe1O_6$) and ($Fe2O_6$) octahedral polyhedra. Since an increase in the $\langle$Fe-O$\rangle$ distance leads generally to an increase in δ value,[24] the Fe1 subspectrum with largest isomer shift δ_1 (Table V) is attributed to the iron ions replacing nickel in larger ($Ni1O_6$) polyhedra, whereas the Fe2 quadrupole doublet corresponds to the Fe^{3+} ions in smaller ($Ni2O_6$) polyhedra.

The noticeably different quadrupole splittings Δ_1 and Δ_2 (Table V) would mean that the Fe^{3+}cations are distributed over nickel sites with significantly different local symmetry. However, within an ionic model,[25] where a monopole lattice contribution (V^{lat}) to the total tensor of the electric field gradient (EFG) at high-spin Fe^{3+} cations is substituted for nickel in the Ni1 and Ni2 positions, our calculations show that for both $R =$ Tm, Yb nickelates, a ratio $V^{lat}_{ZZ}(Fe1)/V^{lat}_{ZZ}(Fe2)$ is close to unity (Table V) (where V_{ZZ} is the main component of the V^{lat} tensor). Crystallographic parameters used in these calculations were taken from our neutron data for the

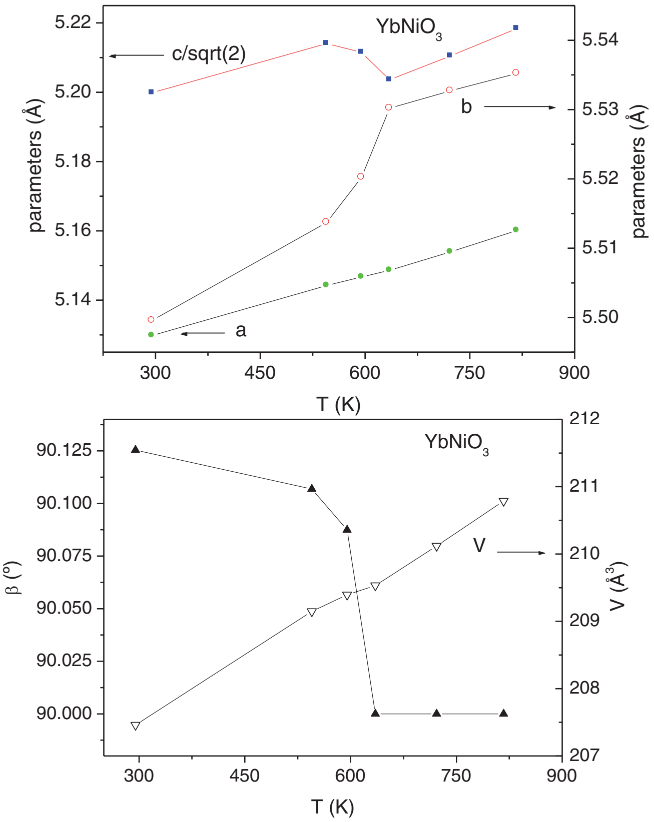

FIG. 8. (Color online) Thermal variation of the unit-cell parameters across the electronic delocalization of YbNiO$_3$ ($T_{\rm MI}$ = 598 K). (a) a, b, and c parameters, and (b) monoclinic β angle and unit-cell volume.

monoclinic-insulating phases of the unsubstituted TmNiO$_3$ and YbNiO$_3$ samples (Tables III and IV). Since $V_{ZZ}(\text{Fe}) \approx 2\Delta_i/2eQ$ (where Q is the ^{57}Fe nuclear quadrupole moment), we have thus a significant discrepancy between theoretical ($\Delta_1^{\rm lat}/\Delta_2^{\rm lat} \approx 1$) and experimental ($\Delta_1/\Delta_2 \gg 1$; Table V) quadrupole splittings. This result indicates the need to consider local valence contributions to the total EFG due to the overlap of $2s/2p$ orbitals of the oxygen O^{2-} anions with the np ($V^{ov}_{ZZ,\rm np}$) and $3d$ ($V^{ov}_{ZZ,\rm 3d}$) orbitals of iron cations, and the covalent charge transfer O$^{2-}(2p^6)$→Fe$^{3+}(3d^5)$ ($V^{ov}_{ZZ,3d}$):[26]

$$V^{\rm tot}_{ZZ} = (1-\gamma_\infty)V^{\rm lat}_{ZZ} + (1-{\rm R})\left(V^{\rm cov}_{ZZ,\rm 3d} + V^{ov}_{ZZ,\rm 3d} + \sum_{\rm n} V^{ov}_{ZZ,\rm np}\right), \qquad (1)$$

where $\gamma_\infty = -9.14$ and $R = 0.32$[26] are Sternheimer factors for these two contributions.

Our calculations (Table VII) clearly show that inclusion of only the overlap contributions $V^{ov}_{ZZ,3d}$ and $V^{ov}_{ZZ,\rm np}$ caused by the local distortions of the (Fe1O$_6$) and (Fe2O$_6$) polyhedra cannot fully explain the observed significant difference in the experimental Δ_1 and Δ_2 values (Table V). The most important contributions $V^{\rm cov}_{ZZ,3d}$ caused by the partial charge transfer O$^{2-}(2p_\sigma)$ →Fe$^{3+}(3d)$ were calculated using the covalency parameters (b_σ^2) shown in Table VII. The resulting absolute values are in qualitative agreement with the covalency parameters ($b_\sigma^2 \approx 0.07 \div 0.09$) for orthoferrites,[27] and their relative values

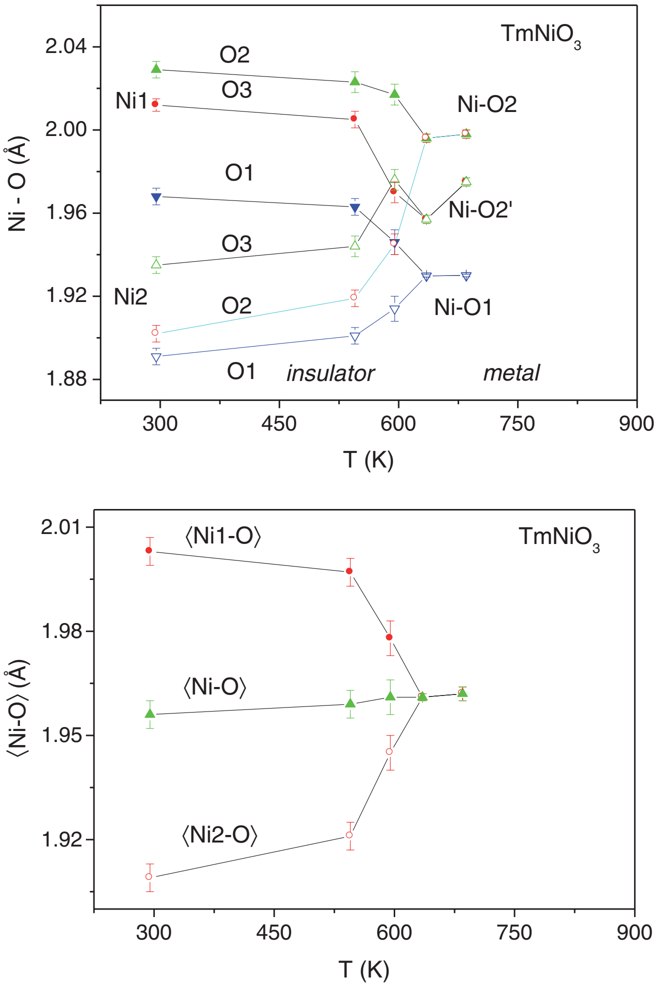

FIG. 9. (Color online) (a) Temperature dependence of individual Ni-O distances and (b) thermal evolution of the average ⟨Ni1-O⟩, ⟨Ni2-O⟩, and ⟨Ni-O⟩ bond lengths of the (NiO$_6$) octahedra for TmNiO$_3$.

[b_σ^2(Fe2) ≫ b_σ^2(Fe1)] indicate that ^{57}Fe^{3+} probe ions are not involved in the charge transfer between nickel Ni1 and Ni2 sites, stabilizing in the smaller (Fe2O$_6$) polyhedra with more covalent Fe2-O bonds and in the larger (Fe1O$_6$) octahedra with more ionic Fe1-O bonds. Since the high-spin Fe$^{3+}(t_2^3e^2)$ ions have no orbital degeneracy, i.e., they cannot induce the additional Jahn-Teller deformation of (FeO$_6$) polyhedra, the observed quadrupole splitting Δ_1 and Δ_2 values for the Fe1 and Fe2 subspectra are the result of a delicate balance among the topology of the monoclinic lattice of RNiO$_3$ nickelates [$V^{\rm lat}_{ZZ}$(Fe1) ≈ $V^{\rm lat}_{ZZ}$(Fe2)], the local oxygen distortion (Δ_d) of the Ni1 and Ni2 sites [$V^{ov}_{ZZ,\rm (3d/np)}$(Fe1) > $V^{ov}_{ZZ,\rm (3d/np)}$(Fe2)], and different covalency of the Fe-O bonds in the (Fe1O$_6$) and (Fe2O$_6$) octahedra.

The temperature dependencies $\delta_{1,2}(T)$ and $\Delta_{1,2}(T)$, shown in Fig. 5, can be divided into three regions. In the first temperature range, the values of isomer shifts and quadrupole splittings of both partial spectra decrease linearly with an increase in temperature. The experimental values of the temperature coefficients ($\partial\delta/\partial T$) for the linear dependencies $\delta_1(T)$ and $\delta_2(T)$ ($\langle\partial\delta/\partial T\rangle \approx -9 \times 10^{-4}$ mm s^{-1} K^{-1}) are in agreement with the corresponding theoretical value for the

TABLE VII. Values of the calculated lattice (V_{ZZ}^{lat}), overlap and covalent ($V_{ZZ,\mathrm{np}}^{ov}$, $V_{ZZ,3d}^{ov/\mathrm{cov}}$) contributions to the principal component (V_{ZZ}^{tot}) of the EFG tensor at the ^{57}Fe sites, covalency parameter (b_{σ}^{2}), and calculated quadrupole splittings (Δ_i^{calc}) in $R\mathrm{Ni}_{0.985}{}^{57}\mathrm{Fe}_{0.015}\mathrm{O}_3$.

R	Sites	V_{ZZ}^{lat}	$V_{ZZ,\mathrm{np}}^{ov}$	$V_{ZZ,3d}^{ov}$	$V_{ZZ,3d}^{\mathrm{cov}}$	b_{σ}^{2}	V_{ZZ}^{tot}	$\lvert\Delta^{\mathrm{cal}}\rvert$
		($\lvert e\rvert$/Å^3)	($\lvert e\rvert$/Å^3)	($\lvert e\rvert$/Å^3)	($\lvert e\rvert$/Å^3)		($\lvert e\rvert$/Å^3)	(mm/s)
Tm	Fe1	−0.13	−1.32	−0.06	5.72	0.02	1.65	0.37
	Fe2	−0.14	−0.28	−0.01	2.43	0.082	0.09	0.02
Yb	Fe1	−0.13	−1.32	−0.06	5.55	0.020	1.54	0.35
	Fe2	−0.12	−0.25	−0.01	2.48	0.079	0.25	0.06

high-temperature Debye approximation for the second-order Doppler shift: -7.3×10^{-4} mm s^{-1} K^{-1}.[24] This behavior indicates that the nickel sublattice undergoes no structural or electronic transitions in the temperature range under consideration.

The second temperature range (Fig. 5) exhibits the gradual equalization of hyperfine parameters δ_1/δ_2 and Δ_1/Δ_2 for the two partial spectra. The greatest changes are observed for the parameters of the Fe2 subspectrum, which corresponds to Fe^{3+} ions replacing nickel in the ($\mathrm{Ni2O_6}$) polyhedra of smallest volume. Therefore, in terms of the hyperfine parameters of ^{57}Fe probe atoms, the Ni2 sites experience the most significant change during the structural phase transition. Figure 11 shows that the temperature dependence of the $\xi \equiv (\delta_1-\delta_2)$ value, characterizing the difference between the main ⟨Fe-O⟩ distances and the covalency parameters of the Fe-O bonds in the ($\mathrm{FeO_6}$) polyhedra, undergoes a gradual decrease with increasing temperature. Since the appearance of the two positions for the iron probe atoms is the result of redistribution of electronic charge in the nickel sublattice, the ξ parameter can be considered as a measure of the degree (σ) of charge disproportionation $2\mathrm{Ni}^{3+}\rightarrow\mathrm{Ni}^{(3+\sigma)+}+\mathrm{Ni}^{(3-\sigma)+}$ or charge ordering in nickel sublattice. Thus, based on the Mössbauer data, we can suggest that the transition $P2_1/n\rightarrow Pbnm$ is continuous and uniform throughout the nickelates structure; i.e., it occurs gradually, affecting simultaneously all Ni1 and Ni2 positions in the nickel sublattice. Moreover, the measurements in the "heating" and "cooling" modes did not reveal any hysteresis in the temperature dependencies of the hyperfine parameters of Fe1 and Fe2 quadrupole doublets. Early, a similar continuous change of the order parameter, typical for the second-order phase transitions,[28] was observed in Mössbauer spectra of $\mathrm{CaFeO_3}$ ferrate,[29–31] where the charge disproportionation $2\mathrm{Fe}^{4+}\rightarrow\mathrm{Fe}^{(4+\sigma)+}+\mathrm{Fe}^{(4-\sigma)+}$ occurs at $T<170$ K.

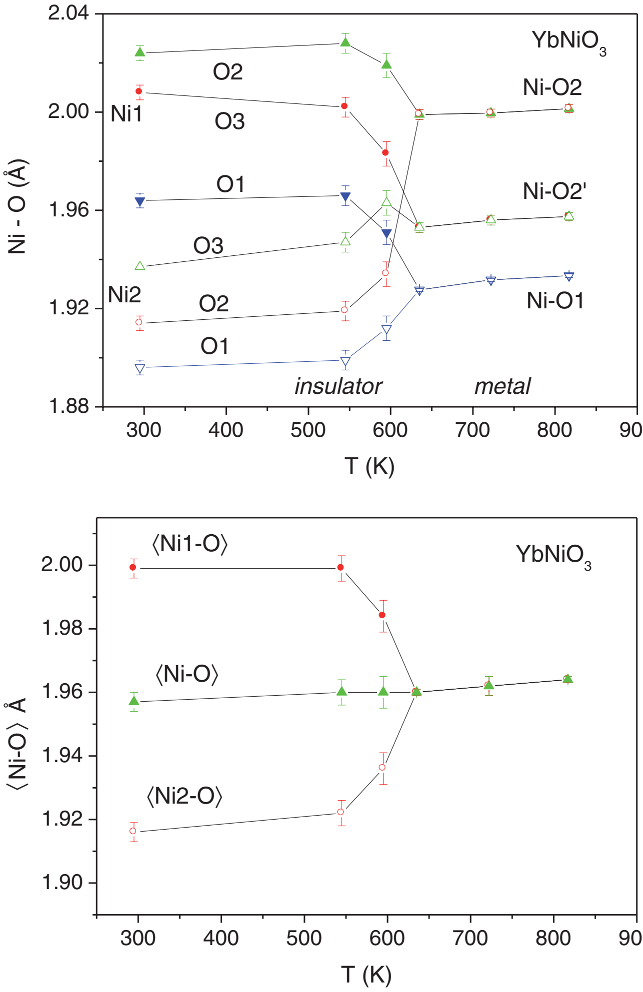

FIG. 10. (Color online) (a) Temperature dependence of individual Ni-O distances and (b) thermal evolution of the average ⟨Ni1-O⟩, ⟨Ni2-O⟩, and ⟨Ni-O⟩ bond lengths of the ($\mathrm{NiO_6}$) octahedra for $\mathrm{YbNiO_3}$.

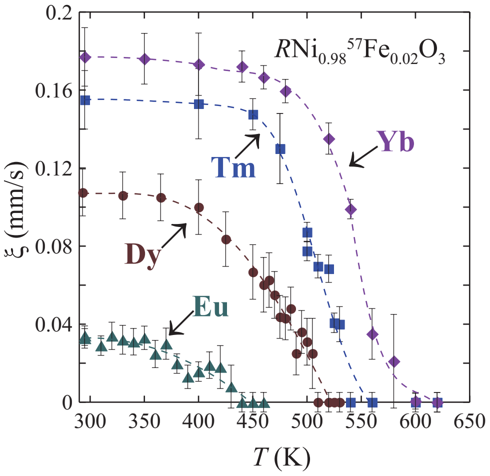

FIG. 11. (Color online) Temperature dependence of the difference of the isomer shifts $\xi=(\delta_1-\delta_2)$ for Fe1 and Fe2 subspectra of $R\mathrm{Ni}_{0.985}{}^{57}\mathrm{Fe}_{0.015}\mathrm{O}_3$ (R = Tm, Yb) and $R\mathrm{Ni}_{0.98}{}^{57}\mathrm{Fe}_{0.2}\mathrm{O}_3$ (data for R = Eu and R = Dy were taken from Refs. 12 and 14, respectively).

Finally, considering the second temperature range, we shall focus on the $\xi(T)$ evolution for the different R^{3+} cations. The $\xi(T)$ values for R = Eu and Dy have been included for the sake of comparison, taken from Refs. 12 and 14. According to Figure 11, at a given temperature, the $\xi(T)$ value increases with decreasing of ionic radius of rare-earth cations Eu→Dy→Tm→Yb. This behavior is correlated with the chemical nature of rare-earth R^{3+} cations bonded with Ni^{3+} cations via the same O^{2-} anions. For smaller and more acid R^{3+} ($Eu^{3+} \to \ldots \to Yb^{3+}$) ions, along the R-O-Ni bonds, the electron density is increasingly kept in the progressively more covalent R-O bonds, thus weakening the Ni-O bonds (narrowing $\sigma^*[e_g]$ band), and, consequently, destabilizing the Ni^{3+} state.

In the third temperature range, $T > T_{MI}$ (Fig. 5), the hyperfine parameters of both subspectra coincide completely. This means that at $T > T_{MI}$, all iron positions become equivalent. The isomer shift δ value decreases linearly with an increase in temperature, with nearly the same temperature coefficient as shifts δ_1 and δ_2 in the first temperature range. An estimation of the quadrupole splitting Δ within the above model, using the crystallographic data obtained for TmNiO$_3$ and YbNiO$_3$ nickelates at $T > T_{MI}$ (Table II), and substituting in Eq. (1) the values of $(S^k_{nl})^2$ and b^2_σ corrected for the experimental ⟨Ni-O⟩ distances, yields $\Delta^{(calc)} = 0.30$ mm s^{-1}, which (in coincidence with the experimental value $\Delta = 0.30 \pm 0.01$ mm s^{-1}) falls in the range between Δ_1 and Δ_2 at $T = 295$ K. This again indicates that the main structural features of the local coordination of probe ^{57}Fe atoms are inherited from the nickel cations in the Ni1 and Ni2 positions, which are replaced by these atoms.

Note that the temperatures above which all iron probe positions become equivalent for the TmNi$_{0.985}$^{57}Fe$_{0.015}$O$_3$ (∼540 K) and YbNi$_{0.985}$^{57}Fe$_{0.015}$O$_3$ (∼580 K) samples are lower than the insulator-metal transition temperatures for TmNiO$_3$ ($T_{MI} \approx 596$ K) and YbNiO$_3$ ($T_{MI} \approx 598$ K). The introduction of probe ^{57}Fe atoms into the structure of RNiO$_3$ nickelates thus lowers the phase-transition temperature by ΔT_{MI}(Tm) ≈ −50 K and ΔT_{MI}(Yb) ≈ −20 K. The similar considerable effect of small amounts of paramagnetic ^{57}Fe atoms on temperature T_{MI} was previously observed for other representative members of the RNiO$_3$ family with R = Nd ($\Delta T_{MI} \approx -45$ K),[15] Eu ($\Delta T_{MI} \approx -50$ K),[12] and Dy ($\Delta T_{MI} \approx -60$ K).[14] This result will be discussed in detail elsewhere.

VI. CONCLUSIONS

The MI transition temperatures of highly distorted TmNiO$_3$ and YbNiO$_3$ perovskites, prepared under high-oxygen pressure, were determined by DSC measurements; they occur well above RT, at $T_{MI} = 596$ and 598 K, respectively. The thermal evolution of the crystal structure of both perovskites shows that these oxides stabilize a charge disproportionation below T_{MI} implying a separation of two kinds of (NiO$_6$) octahedra (large Ni1O$_6$ and small Ni2O$_6$) described in a pseudo-orthorhombic unit cell characterized by a subtle monoclinic distortion ($\beta \sim 90.12°$ at RT) in the $P2_1/n$ space group. Whereas the (Ni1O$_6$) octahedron is significantly distorted, (Ni2O$_6$) is much more regular. This is consistent with a scenario considering that the former contains more ionic Ni-O bonds and is susceptible to experience a Jahn-Teller deformation, whereas the small (Ni2O$_6$) octahedron is constituted by more covalent Ni-O bonds. Above T_{MI}, TmNiO$_3$ and YbNiO$_3$ become orthorhombic, e.g., *Pbnm*. The ^{57}Fe Mössbauer spectra of the iron-doped TmNiO$_3$ and YbNiO$_3$ samples at $T < T_{MI}$ indicate the stabilization of the Fe^{3+} probe cations in two Fe1 and Fe2 octahedral positions, replacing the nickel in Ni1 and Ni2 sites. The calculations of EFG, using the crystal parameters for undoped samples, show that the quadrupole splittings for Fe1 and Fe2 subspectra reflect features of the monoclinic crystal structure of RNiO$_3$ nickelates. The Mössbauer data at $T \approx T_{MI}$ suggest that the transition $P2_1/n \to Pbnm$ is typical for second-order phase transitions. The measurements in the "heating" and "cooling" modes did not reveal any hysteresis in the temperature dependencies of the hyperfine parameters of Fe1 and Fe2 quadrupole doublets. At $T > T_{MI}$, the ^{57}Fe spectra demonstrate the formation of a unique state for the Fe^{3+} probe cations that clearly indicates the complete disappearance of charge disproportionation above the insulator-metal phase transition.

ACKNOWLEDGMENTS

We thank the Spanish Ministry of Education under the project MAT2010-16404, and the Russian Foundation for Basic Research (Ref. No 13-02-00196) for financial support. We are grateful to ILL for making all facilities available.

---

[*] Corresponding author: ja.alonso@icmm.csic.es

[1] J. B. Torrance, P. Lacorre, A. I. Nazzal, E. J. Ansaldo, and Ch. Niedermayer, Phys. Rev. B **45**, 8209 (1992).

[2] G. Démazeau, A. Marbeuf, P. Pouchard, and P. Hagenmuller, J. Solid State Chem. **3**, 582 (1971).

[3] J. A. Alonso, J. L. García-Muñoz, M. T. Fernández-Díaz, M. A. G. Aranda, M. J. Martínez-Lope, and M. T. Casais, Phys. Rev. Lett. **82**, 3871 (1999).

[4] J. A. Alonso, M. J. Martínez-Lope, M. T. Casais, M. A. G. Aranda, and M. T. Fernández-Díaz, J. Am. Chem. Soc. **121**, 4754 (1999).

[5] J. A. Alonso, M. J. Martínez-Lope, M. T. Casais, J. L. García-Muñoz, and M. T. Fernández-Díaz, Phys. Rev. B **61**, 1756 (2000).

[6] J. A. Alonso, M. J. Martínez-Lope, M. T. Casais, J. L. García-Muñoz, M. T. Fernández-Díaz, and M. A. G. Aranda, Phys. Rev. B **64**, 094102 (2001).

[7] M. Medarde, C. Dallera, M. Grioni, B. Delley, F. Verney, J. Mesot, M. Sikora, J. A. Alonso, and M. J. Martínez-Lope, Phys. Rev. B **80**, 245105 (2009).

[8] I. Mazin, D. I. Khomskii, R. Lengsdorf, J. A. Alonso, W. G. Marshall, R. M. Ibberson, A. Podlesnyak, M. J. Martínez-Lope, and M. M. Abd-Elmeguid, Phys. Rev. Lett. **98**, 176406 (2007).

[9] J. S. Zhou and J. B. Goodenough, Phys. Rev. B **69**, 153105 (2004).

[10] S. J. Kim, G. Démazeau, I. A. Presniakov, K. V. Pokholok, A. V. Sobolev, and N. S. Ovanesyan, J. Am. Chem. Soc. **123**, 8127 (2001).

[11] S. J. Kim, G. Démazeau, I. A. Presniakov, K. V. Pokholok, A. V. Baranov, and A. V. Sobolev, J. Solid State Chem. **168**, 126 (2002).

[12] I. A. Presniakov, A. V. Baranov, G. Démazeau, V. S. Rusakov, A. V. Sobolev, J. A. Alonso, M. J. Martínez-Lope, and K. Pokholok, J. Phys.: Condens. Matter **19**, 036201 (2007).

[13] S. J. Kim, G. Démazeau, I. A. Presniakov, K. V. Pokholok, A. V. Baranov, A. V. Sobolev, D. A. Pankratov, and N. S. Ovanesyan, Phys. Rev. B **66**, 014427 (2002).

[14] J. A. Alonso, M. J. Martínez-Lope, G. Démazeau, M. T. Fernández-Díaz, I. A. Presniakov, V. S. Rusakov, T. V. Gubaidulina, and A. V. Sobolev, Dalton Trans. 6584 (2008).

[15] I. A. Presniakov, G. Démazeau, A. V. Baranov, A. V. Sobolev, and K. V. Pokholok. Phys. Rev. B **71**, 054409 (2005).

[16] A. Caytuero, H. Micklitz, M. M. Abd-Elmeguid, F. J. Litterst, J. A. Alonso, and A. Baggio-Saitovitch, Phys. Rev. B **76**, 193105 (2007).

[17] H. M. Rietveld, J. Appl. Crystallogr. **2**, 65 (1969).

[18] J. Rodríguez-Carvajal, Physica B **192**, 55 (1993).

[19] V. S. Rusakov, Bull. Russian Acad. Sci. Phys. **63**, 1093 (1999).

[20] M. E. Matsnev, and V. S. Rusakov, SpectrRelax, AIP Conf. Proc. **1489**, 178 (2012).

[21] M. Medarde, P. Lacorre, K. Conder, F. Fauth, and A. Furrer, Phys. Rev. Lett. **80**, 2397 (1998).

[22] S. J. Kim, M. J. Martínez-Lope, M. T. Fernandez-Diaz, J. A. Alonso, I. Presniakov, and G. Démazeau, Chem. Mater. **14**, 4926 (2002).

[23] R. D. Shannon, Acta Crystallogr. A **32**, 751 (1976).

[24] F. Menil, J. Phys. Chem. Solids **46**, 763 (1985).

[25] I. A. Presniakov, V. S. Rusakov, T. V. Gubaidulina, A. V. Sobolev, A. V. Baranov, G. Démazeau, O. S. Volkova, V. M. Cherepanov, E. A. Goodilin, A. V. Knot'ko, and M. Isobe, Phys. Rev. B **76**, 214407 (2007).

[26] R. R. Sharma, Phys. Rev. B **6**, 4310 (1972).

[27] G. A. Sawatzky and F. Wan der Woude, J. Physique **35**, C6-47 (1974).

[28] D. Khomskii, *Basic Aspects of the Quantum Theory of Solids* (Cambridge University Press, New York, 2011).

[29] M. Takano, N. Nakanishi, Y. Takeda, S. Naka, and T. Takeda, Mater. Res. Bull. **12**, 923 (1977).

[30] M. Takano, S. Nasu, T. Abe, K. Yamamoto, S. Endo, Y. Takeda, and J. B. Goodenough. Phys. Rev. Lett. **67**, 3267 (1991).

[31] M. Takano and Y. Nakeda, Bull. Inst. Chem. Res. Kyoto Univ. **61**, 406 (1983).